A ballistic limit analysis programme for shielding against micrometeoroids and orbital debris ☆

S. Ryan [a,*], E.L. Christiansen [b]

[a] Defence Science and Technology Organisation, Australia
[b] NASA Johnson Space Center, USA

ARTICLE INFO

ABSTRACT

A software programme has been developed that enables the user to quickly and simply perform ballistic limit calculations for common spacecraft structures that are subjected to hypervelocity impact of micrometeoroid and orbital debris (MMOD) projectiles. This analysis programme consists of two core modules: design and performance. The design module enables a user to calculate preliminary dimensions of a shield configuration (e.g. thicknesses/areal densities, spacing, etc.) for a "design" particle (diameter, density, impact velocity, and incidence). The performance module enables a more detailed shielding analysis, providing the particle size that is "stopped" by a user-defined shielding configuration over the range of relevant in-orbit impact conditions.

© 2011 Elsevier Ltd. All rights reserved.

1. Introduction

Ballistic limit equations (BLEs) define the failure limits of a structure in terms of impactor properties such as diameter, velocity, angle, etc. They are used in spacecraft mission risk assessment to determine the probabilities of penetration of the spacecraft's shielding from the MMOD flux. Due to the complexity of damage mechanisms and material behaviour at pressures and strain rates generated during hypervelocity impact, BLEs are often highly empirical. An example of a multi-wall shield ballistic limit equation from Ref. [1], expressed as critical projectile diameter d_c, in terms of velocity V, and impact angle θ, is provided.

At low velocities, i.e. $V \leq 2.7 \cos(\theta)^\beta$,

$$d_c = [m_p(\theta)V_{LV}(\theta)^{5/3} + n(\theta)V_{LV}(\theta)^{2/3}]V(\theta)^{-2/3} \tag{1}$$

Intermediate velocities, i.e. $2.7 \cos(\theta)^\beta < v < 6.5 \cos(\theta)^\gamma$,

$$d_c = [m(\theta)V(\theta) + n(\theta)] \tag{2}$$

At hypervelocities, i.e. $V \geq 6.5 \cos(\theta)^\gamma$,

$$d_c = [m(\theta)V_{HV}(\theta)^{4/3} + n(\theta)v_{HV}(\theta)^{1/3}]v(\theta)^{-1/3} \tag{3}$$

where V_{LV} and V_{HV} are the threshold velocities between the low- and intermediate-velocity regimes, and the intermediate and hypervelocity regimes, respectively. The functions $m(\theta)$ and $n(\theta)$ are given as

$$m(\theta) = \begin{cases} a_1(\theta) + b_1, & \text{if } \theta \leq \pi/4 \\ a_2(\theta) + b_2, & \text{if } \theta > \pi/4 \end{cases} \tag{4}$$

$$n(\theta) = \begin{cases} c_1(\theta) + d_1, & \text{if } \theta \leq \pi/4 \\ c_2(\theta) + d_2, & \text{if } \theta > \pi/4 \end{cases} \tag{5}$$

In Eqs. (1)–(5) the terms β, γ, a_1, b_1, c_1, d_1, a_2, b_2, c_2, and d_2 are all empirically fitted to the test data.

The majority of generalised BLEs are based on Christiansen's new non-optimum (NNO) equation [2], which is itself based on the BLE of Cour-Palais for non-optimum bumper-to-projectile geometry impacts [3]. Although based on the NNO, modified equations often fail to maintain the validity

---

Nomenclature

AD	areal density (g/cm^2)
C	sound speed (km/s)
d	diameter (cm)
D_c	crater diameter (cm)
D_h	clear hole diameter (cm)
HB	Brinell hardness (BN)
m	mass (g)
P	penetration depth (cm)
S	spacing between shield elements (cm)
t	thickness (cm)
V	impact velocity (km/s)
ρ	density (g/cm^3)
θ	impact angle (0° corresponds to impact perpendicular to the target surface) (deg.)

σ_y	yield strength (ksi)
A	aluminium bumper (hybrid MS)
Al	aluminium
b	bumper plate
b2	2nd bumper plate (MDB)
c	critical
f	fabric layer
HV	hypervelocity regime limit
LV	low velocity regime limit
ob	outer bumper
p	projectile
s	shield
SIP	strain isolation pad
T	tile
w	rear wall
∞	semi-infinite

bounds or application guidelines of the original equation. For example, the NNO defines a cut-off impact angle of 65° (measured perpendicular to the target surface), above which an increase in obliquity does not affect the calculated failure limit, i.e. $d_c(\theta > 65°) = d_c(\theta = 65°)$, or $t_w(\theta > 65°) = t_w(\theta = 65°)$. For example, the ESA triple-wall [4], and modified ESA triple-wall (MET) [5], although based on the NNO, do not include any limit of effective obliquity nor do they present data to support the extension.

In addition to their use in mission risk assessments, BLEs can be useful tools for performing preliminary sizing estimates, comparing the performance of difference shield types, and estimating the effect of parameter variations on shield performance or required thicknesses. However, the complexity of the equations together with inconsistent (or lacking) validation and poor documentation means that their correct application can be difficult. Even expert users, when presented with the same problem, can often return widely varying predictions. In order to increase the usability of ballistic limit equations for common spacecraft structures, a software programme has been developed at NASA Johnson Space Centre that allows the user to quickly and simply perform ballistic limit calculations for preliminary shield sizing or performance assessment. In this paper, an overview of the programme capabilities is presented, along with a discussion of selected ballistic limit equations underlying the programme outputs.

2. Programme overview

The analysis programme operates as an add-in to Microsoft Excel® and contains two core modules: a design module and a performance module. The design module enables a user to calculate preliminary dimensions of a shield configuration (e.g. thickness/areal densities, spacing, etc.) for a "design" particle (diameter, density, impact velocity, and incidence). The performance module enables a more detailed shielding analysis, providing the performance of a user-defined shielding configuration over the range of relevant in-orbit impact conditions. The programme is operated via a graphical user interface (e.g. see Fig. 1), and is

distributed with a comprehensive user's manual [6] that can be accessed within the programme help file.

For each configuration included in the analysis programme, the BLE applied has been selected (in the case of multiple options) based on a competitive evaluation of equation accuracy against existing test data. Furthermore, although it is not possible to fully verify any BLE through ground-based testing due to launcher limitations, an effort has been made to identify the limits of applicability, either directly from author publications, or through details of the empirical derivation/experimental validation applied. A discussion on the source of empirical constants, and a summary of validated application limits constants is provided for each BLE.

3. Ballistic limit equations

3.1. Single wall

Analysis capability is provided for metallic (aluminium, titanium, and stainless steel), composite (CFRP, fibreglass), and transparent (fused silica glass, fused quartz glass, polycarbonate) single wall structures.

3.1.1. Aluminium single wall

The Cour-Palais semi-infinite plate equation considers the impact of a projectile on a semi-infinite plate that results in the formation of a hemispherical crater. As the thickness of the plate is decreased, the plate undergoes internal fracturing (incipient spallation), detachment of spalled material, and finally perforation when the entry crater and spallation area overlap. The penetration depth of a semi-infinite target is calculated (from Ref. [7]) as

$$P_\infty = 5.24 d_p^{19/18} HB^{-1/4} (\rho_p/\rho_s)^\alpha (V \cos\theta/C)^{2/3} \qquad (6)$$

where

$$\alpha = \begin{cases} 0.5, & \text{if } (\rho_p/\rho_s) < 1.5 \\ 2/3 & \text{if } (\rho_p/\rho_s) \geq 1.5 \end{cases}$$
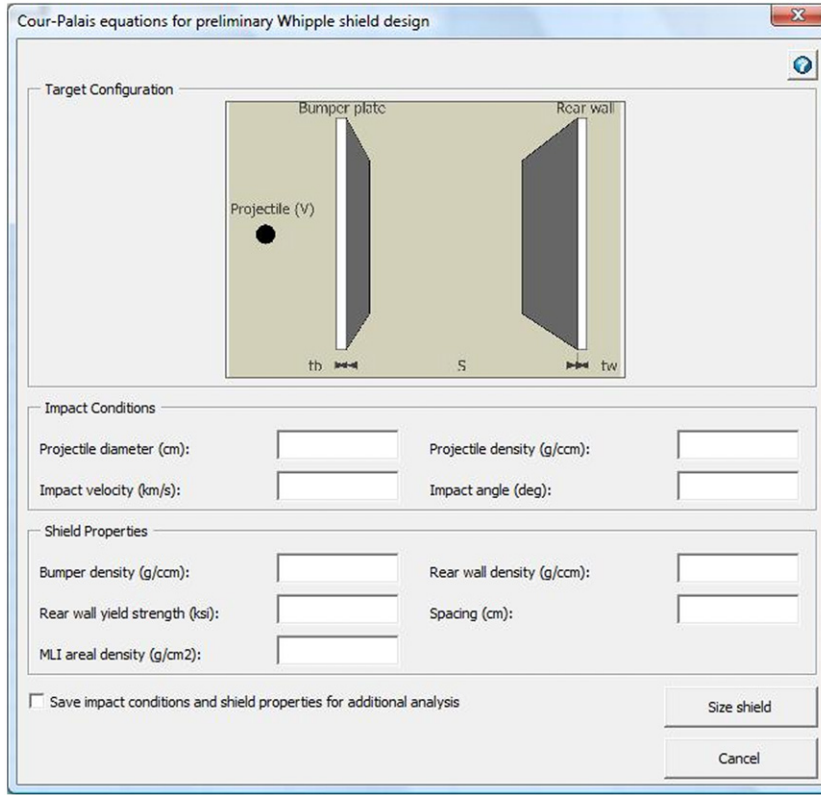
Fig. 1. Example of the graphical user interface (preliminary sizing of a metallic Whipple shield).

Required shielding thickness can be determined for a design particle, depending on the failure mode:

to prevent incipient spallation: $\quad t_s \geq 3.0 P_\infty$ (7)

to prevent detached spallation: $\quad t_s \geq 2.2 P_\infty$ (8)

to prevent perforation: $\quad t_s \geq 1.8 P_\infty$ (9)

For a specific shielding configuration, the ballistic limit can be determined using

$$d_c = \left[\frac{t_s}{k} \frac{HB^{1/4}(\rho_s/\rho_p)^{\alpha}}{5.24(V\cos\theta/C)^{2/3}} \right]^{18/19}$$ (10)

where $k = 3.0$, 2.2, 1.8 for incipient spall, detached spall, and perforation, respectively.

An overview of the Cour-Palais semi-infinite plate equation's validation basis for use with aluminium single wall structures is provided in Ref. [6].

3.1.2. Titanium single wall

Penetration into a monolithic titanium shield is calculated with a slightly modified version of the Cour-Palais semi-infinite relationship, from Ref. [8] as

$$P_\infty = 5.24 d_p HB^{-1/4}(\rho_p/\rho_s)^{1/2}(V\cos\theta/C)^{2/3}$$ (11)

The thickness scaling factor, k, is also modified for titanium single walls, equal to 3.0, 2.4, and 1.8 for incipient spall, detached spall, and perforation, respectively.

Performance of a single titanium wall is predicted using

$$d_c = \frac{t_s}{k} \frac{HB^{1/4}(\rho_s/\rho_p)^{1/2}}{5.24(V\cos\theta/C)^{2/3}}$$ (12)

Modifications to the Cour-Palais semi-infinite plate cratering relationship were made for monolithic titanium based on testing of the James Webb Space Telescope (JWST). Derivation was made from test data on rod and sheet stock Ti 15-3-3-3 at normal incidence and impact velocities that were between 6.4 and 7.0 km/s. Numerical simulation data presented in Ref. [8] was used for verification.

3.1.3. Stainless steel single wall

Penetration relationships for monolithic stainless steel targets are provided in Ref. [9], which is derived from cratering experiments using CRES 15-5PH targets. Material properties used in the aluminium and titanium alloy relationships (i.e. Brinell hardness and sound speed) are included in the material parameter K, which is equal to 0.345. Penetration depth into a semi-infinite target is calculated as

$$P_\infty = K d_p^{19/18}(\rho_p/\rho_s)^{1/2}(V\cos\theta/C)^{2/3}$$ (13)

To prevent perforation, the required thickness of the panel must be equal to or greater than 1.8 times the penetration depth calculated by Eq. (6) (i.e. $t_s \geq 1.8 P_\infty$). For a specific shielding configuration, the ballistic limit

can be determined using

$$d_c = \left[\frac{t_s}{0.621} \frac{(\rho_s/\rho_p)^{1/2}}{(V\cos\theta/C)^{2/3}} \right]^{18/19} \qquad (14)$$

3.1.4. CFRP single wall

Crater formation and shock transmission in multi-layer, non-isotropic materials such as CFRP is considerably different to that seen in metals. Schaefer et al. [5] proposed a modification of the Cour-Palais cratering equation (Eq. (6)) that uses a single material parameter (K_{CFRP}) to describe the effect of material properties (e.g. Brinell hardness, density, and sound speed). This factor is empirically adjusted to impact test data. To extend the application of this equation, a modified version is applied which explicitly includes the effect of shield density (based on Cour-Palais' semi-infinite plate relationship). The material parameter K_{CFRP} derived by Schaefer et al. for the material tested in Ref. [5] (i.e. $\rho_s = 1.42$ g/cm^3), is subsequently adjusted to fit the predictions of the original equation, yielding $K_{CFRP} = 0.62$. The modified equation is given as

$$P_\infty = K_{CFRP} d_p (\rho_p/\rho_s)^{1/2} (V\cos\theta)^{2/3} \qquad (15)$$

The required shield thickness to prevent detached spallation and perforation is 3.0 and 1.8 times the penetration depth, respectively (i.e. $k = 3.0, 1.8$). The performance of a CFRP single wall structure is evaluated using

$$d_c = \frac{t_s}{k} \frac{(\rho_s/\rho_p)^{1/2}}{K_{CFRP}(V\cos\theta)^{2/3}} \qquad (16)$$

Schaefer et al. [5] derived a value of $K_{CFRP} = 0.52$ from a series of seven impact tests on a 3.8 mm thick, intermediate modulus, quasi-isotropic laminate. No further testing has been performed to support the extraction of shield density from the K_{CFRP} constant, and as such the equation should be applied with caution, particularly when the density varies substantially from that of the verification material ($\rho_s = 1.42$ g/cm^3).

3.1.5. Fibreglass single wall

The semi-infinite cratering equation has been modified in Ref. [9] for e-glass/epoxy composite plates based on limited test data (from Ref. [10]). Penetration depth is calculated as

$$P_\infty = K d_p (\rho_p/\rho_s)^{0.5} (V\cos\theta/C)^{2/3} \qquad (17)$$

For the fibreglass laminate that was tested ($\rho_s = 1.8$ g/cm^3), the material constant is $K = 0.434$. To prevent perforation, the required thickness of the panel must be equal to or greater than 1.8 times the penetration depth. The performance of a specific fibreglass single wall structure is evaluated using

$$d_c = \frac{t_s (\rho_p/\rho_s)^{1/2}}{0.781 (V\cos\theta)^{2/3}} \qquad (18)$$

The fibreglass BLE was derived by testing fibreglass replicates of Shuttle Reinforced Carbon–Carbon (RCC) panels as part of the Return to Flight hypervelocity impact testing. These tests were performed at various impact angles, with a constant impact velocity of 6.8 km/s.

3.1.6. Glass

The low tensile strength and brittle nature of glass leads to extensive internal fracturing and surface spallation with shallow crater depths (compared to monolithic metal plates). Impact craters generally have a central area of high damage that can appear white in colour, surrounded by circular fracture patterns. Internal fracturing can also be observed within glass targets that are below the crater limits, the depth of which is of interest for fracture analysis. Crater diameter and depth measurements are shown in Fig. 2 on a fused silica glass target with typical high-velocity impact damage features.

BLEs for fused silica glass were developed during the Apollo Programme to assess the risk that was associated with the crew module windows. Fused quartz glass is used, for instance, in place of fused silica glass on Russian components of the ISS. The primary difference between the two materials arises from the difference in manufacturing
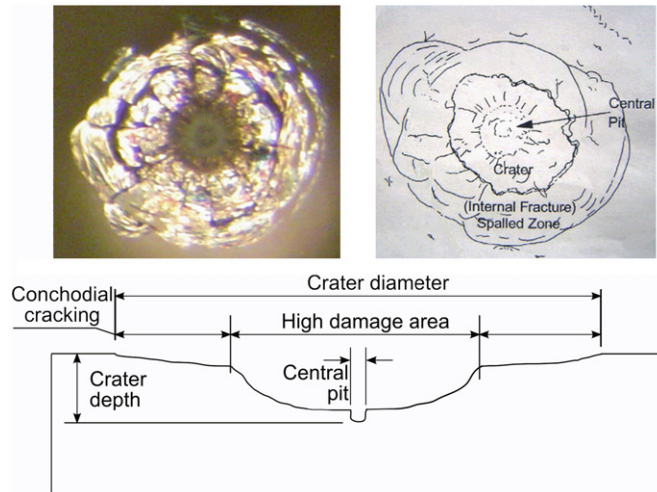

Fig. 2. Damage characteristics and measurements in glass targets.

techniques where fused quartz is manufactured from quartz crystals, and fused silica glass is produced using high-purity silica sand.

The penetration characteristics of the two glasses are slightly different, as defined

$$P_\infty = K d_p^{19/18} \rho_p^{1/2} (V\cos\theta)^{2/3} \tag{19}$$

Where $K=0.53$ for fused silica glass [11] and 0.758 for fused quartz glass [12].

The required thickness of a single wall glass target varies with the defined failure limit, i.e.

to prevent perforation: $\quad t_s \geq 2.0 P_\infty \tag{20}$

to prevent spallation: $\quad t_s \geq 3.0 P_\infty \tag{21}$

to prevent cracking: $\quad t_s \geq 7.0 P_\infty \tag{22}$

For a specific shielding configuration, the ballistic limit can be determined using

$$d_c = \left[\frac{K t_s}{k \rho_p^{1/2} (V\cos\theta)^{2/3}} \right]^{18/19} \tag{23}$$

where $K=1.89$ for fused silica glass and 1.32 for fused quartz glass.

Non-perforating damages on glass structures (e.g. an optical measurement device) can also be considered as a failure criterion if the local surface damage exceeds an operational requirement. The crater diameter can be predicted using

$$D_c = K \rho_p^{0.44} d_p^{1.33} (V\cos\theta)^{0.44} \tag{24}$$

where $K=30.9$ for fused silica glass [13] and 15.1 for fused quartz glass [12].

To calculate the critical particle size based on allowable impact crater diameter ($D_{c,\max}$), Eq. (24) is rearranged as follows:

$$d_c = \left[\frac{D_{c,\max}}{K \rho_p^{0.44} (V\cos\theta)^{0.44}} \right]^{3/4} \tag{25}$$

A considerable amount of test data for HVI on fused silica glass exists as a result of its application on NASA spacecraft (e.g. Apollo, shuttle, ISS, etc.). Impact test data covers a range of projectile materials, impact velocities, and impact angles (see e.g. Ref. [14]). A series of nine HVI tests performed at the NASA Johnson Space Centre (JSC) on fused quartz glass, manufactured by the Russian Institute of Technical Glass (Moscow), was used to modify the semi-infinite cratering equation coefficient (0.758) and front side crater diameter equation coefficient (15.1).

3.1.7. Polycarbonate

Polycarbonates are commonly used as protective covers for more fragile glass windows (e.g. ISS hatch windows) due to their significantly higher impact strength and abrasion resistance. Due to these features, the penetration depth of polycarbonate is less than that of glass or acrylic. The thickness of polycarbonate required to defeat a design projectile is calculated (from Ref. [14]) as

$$t_s = 0.64 k d_p \rho_p^{1/3} V^{2/3} (\cos\theta)^{1/3} \tag{26}$$

where $k=1.50$, 1.6, and 2.4 for perforation, detached spall, and incipient spall, respectively.

For performance evaluations, Eq. (19) is rearranged as

$$d_c = \frac{t_s}{0.64 k \rho_p^{1/3} V^{2/3} (\cos\theta)^{1/3}} \tag{27}$$

Eqs. (18) and (19) were derived from a series of eight impact tests on Hyzod AR polycarbonate at normal impact and 45° with a limited velocity range.

3.2. Dual-wall

Analysis capability is provided for metallic Whipple shields and honeycomb sandwich panels (aluminium or CFRP facesheets).

3.2.1. Metallic Whipple shield

A Whipple shield consists of a thin sacrificial bumper and rear wall, with some interior spacing, as shown in Fig. 3. Bumper and rear wall thicknesses for defeating a design particle are sized with the new non-optimum (NNO) shield equation [2] for a bumper-thickness-to-projectile-diameter ratio that is optimised for projectile fragmentation and dispersion (only valid for impact velocities > 7 km/s)

$$t_b = c_b d_p \frac{\rho_p}{\rho_b} \tag{28}$$

where $c_b=0.25$ when $15 > S/d_p < 30$ and 0.20 when $S/d_p \geq 30$ (for aluminium on aluminium).

$$t_w = \frac{c_w d_p^{1/2} (\rho_p \rho_b)^{1/6} m_p^{1/3} (V\cos\theta)}{S^{1/2} (\sigma_y/70)^{1/2}} \tag{29}$$

where $c_w=0.16$ cm^2 sec/g$^{2/3}$ km (for al-on-al).

For performance evaluations the ballistic limit of a Whipple shield is defined in three parts, each of which corresponds to a projectile state following impact with the bumper plate. The low-velocity (LV) regime is defined for impacts in which the projectile perforates the bumper plate without fragmenting, leading to impact of an intact (albeit deformed) projectile on the shield rear wall. Once impact velocities are increased such that shock amplitudes are sufficient to induce projectile fragmentation, this is termed the intermediate (or shatter) regime.

Within the shatter regime, increases in velocity lead to additional projectile fragmentation (and eventually melting), providing a more equally dispersed fragment cloud of
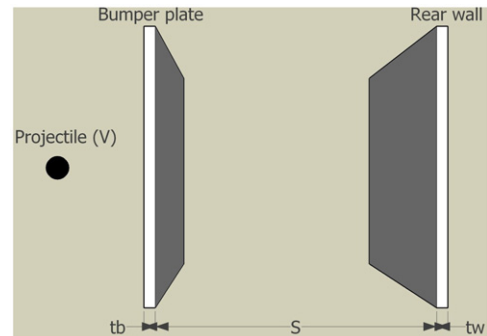

Fig. 3. Metallic Whipple shield configuration.

smaller particles with increasing velocity that is progressively less lethal to the shield rear wall (shielding performance thus increases with impact velocity in the shatter regime). The onset of the hypervelocity (HV) regime is defined as the point at which further increases in impact velocity lead to a reduction in performance of the Whipple shield (i.e. increased fragment cloud lethality). The performance equation used in the analysis programme is based on the NNO BLE [2] and incorporates a selection of modifications proposed in Ref. [15].

In the low velocity regime, i.e. $V \leq V_{LV} \cos \theta$,

$$d_c = \left[\frac{t_w(\sigma_y/40)^{1/2} + t_b}{0.6(\cos\theta)^{5/3}\rho_p^{1/2}V^{2/3}} \right]^{18/19} \tag{30}$$

where

$$V_{LV} = \begin{cases} 1.436(t_b/d_p)^{-1/3}, & \text{for } t_b/d_p < 0.16 \\ 2.60, & \text{for } t_b/d_p \geq 0.16 \end{cases}$$

In the hypervelocity regime, i.e. $V \geq 7\cos\theta$,

$$d_c = 3.918F_2^* \frac{t_w^{2/3}S^{1/3}(\sigma_y/70)^{1/3}}{\rho_p^{1/3}\rho_b^{1/9}(V\cos\theta)^{2/3}} \tag{31}$$

The term F_2^* acts as a de-rating factor for configurations with insufficiently thick bumpers, and is calculated as

$$F_2^* = r_{S/D} - 2\frac{(t_b/d_p)}{(t_b/d_p)_{crit}}(r_{S/D}-1) + \left(\frac{(t_b/d_p)}{(t_b/d_p)_{crit}}\right)^2(r_{S/D}-1) \tag{32}$$

where

$$(t_b/d_p)_{crit} = \begin{cases} 0.2, & \text{for } S/d_p \geq 30 \\ 0.25, & \text{for } S/d_p < 30 \end{cases}$$

and

$$r_{S/D} = \frac{t_w(t_b=0)}{t_w(t_b/d_p=(t_b/d_p)_{crit})}$$

Eq. (32) is valid for the case $(t_b/d_p) < (t_b/d_p)_{crit}$. For configurations with bumper thickness to projectile diameter ratios above the critical limit, the de-rating factor F_2^* converges to the NNO solution (i.e. $F_2^*=1$).

For $V_{LV}\cos\theta < V < 7\cos\theta$ (i.e. intermediate regime), linear interpolation is used. For oblique impact, Christiansen [2] found that at angles above 65°, the majority of rear wall damage is induced by bumper fragments. As such, for higher angles of obliquity, the critical particle size and required rear wall thickness should be constrained at 65°.

A considerable database of HV impact test results exists for metallic Whipple shields (see e.g. [16]). These experiments cover a range of projectile diameters (0.04–1.9 cm), projectile materials (Nylon, glass, and aluminium), impact velocities (6.7–7.5 km/s), bumper thickness to projectile diameter ratios (0.08–0.64), and shield spacing to projectile diameter ratios (13–96). All tests were performed on aluminium alloys at normal incidence ($\theta=0°$), at or close to the target ballistic limit. For the Reimerdes modifications, eight additional tests were performed on targets below the $(t_b/d_p)_{crit}$ limit.

3.2.2. Honeycomb sandwich panel

The Schaefer Ryan Lambert (SRL) triple-wall BLE [17,18] is applicable for dual- and triple-wall structures. To enable this, the equation converges to a dual-wall solution in the case of zero rear wall thickness ($t_w=0$) or zero spacing between the second bumper plate and the rear wall ($S_2=0$). The equation incorporates fit factors (K_{3S}, K_{3D}) from the European Space Agency (ESA) triple-wall equation [4] to account for the presence of the honeycomb core. For sizing the facesheets of a honeycomb sandwich panel, equal thicknesses are assumed, i.e.

$$t_b = t_w = 0.8056 \frac{d_p^{3/2}K_{3D}\rho_p^{1/2}\rho_b^{1/6}V(\cos\theta)^{3\delta/2}}{S^{1/2}(\sigma_y/70)^{1/2}} \tag{33}$$

where $K_{3D}=0.4$ and

$$\delta = \begin{cases} 4/3 & \text{if } 45 \geq \theta \leq 65° \\ 5/4 & \text{if } 45 < \theta > 65° \end{cases} \quad \text{for aluminium}$$
$$\delta = 4/3 \text{ for CFRP}$$

For non-metallic facesheets (e.g. CFRP), areal density-equivalent aluminium facesheet thicknesses are used, i.e.

$$t_{al,eq} = t_{CFRP}\frac{\rho_{CFRP}}{\rho_{Al}} \tag{34}$$

The performance of a honeycomb sandwich panel is determined in three regimes, similar to the BLE described in Section 3.2.1. In the low velocity regime, i.e. $V \leq V_{LV}\cos\theta$,

$$d_c = \left[\frac{t_w/K_{3S}(\sigma_y/40)^{1/2} + t_b}{0.6(\cos\theta)^\delta \rho_p^{1/2}V^{2/3}} \right]^{18/19} \tag{35}$$

where $K_{3S}=1.1$ for CFRP facesheets and 1.4 for aluminium.

In the hypervelocity regime, i.e. $V \geq V_{HV}\cos\theta$,

$$d_c = \frac{1.155t_w^{2/3}S^{1/3}(\sigma_y/70)^{1/3}}{K_{3D}^{2/3}\rho_p^{1/3}\rho_b^{1/9}V^{2/3}(\cos\theta)^\delta} \tag{36}$$

Linear interpolation is used in the intermediate regime, i.e. $V_{LV}\cos\theta < V < V_{HV}\cos\theta$. Impact regime transition velocities (V_{LV}, V_{HV}) are dependent on the outer bumper and projectile material, defined as 3 and 7 km/s for aluminium, and 4.2 and 8.4 km/s for CFRP.

The SRL equation was adjusted using approximately 200 impact tests on various dual- and triple-wall structures. For CFRP, approximately 90 impact tests were performed on six different sandwich panel configurations and aluminium plates for the rear wall [17]. The tests were performed with impact velocities ranging from 2 to 8 km/s, at three different impact angles (0°, 45°, and 60°). For aluminium targets, about 110 impact experiments were used including both aluminium Whipple shields and honeycomb sandwich panels [18]. The impact experiments used representative space hardware for the rear wall structure (e.g. CFRP overwrapped pressure vessels, fuel pipes, heat pipes, etc.).

3.3. Triple-wall

For triple-wall configurations (e.g. metallic triple-wall, sandwich panel, and pressure hull, etc.), the SRL triple-wall BLE is applied. Assuming an equal thickness of the outer and inner bumper plates (i.e. $t_{ob}=t_b$), the performance

of a triple-wall shield described by the SRL equation improves as mass is concentrated in the rear wall (i.e. $t_b/t_w \to 0$). Similarly, as total spacing is biased more towards bumper spacing (i.e. $S_1/S_2 \to \infty$) the shield performance also increases (for $S_{total}/t_{total} \le 30$). As the thicknesses of the inner bumper and rear wall are coupled in the SRL triple-wall equation for impacts at HV, the bumper plate is sized as a percentage of rear wall thickness, the lower limit of which is restricted based on available test data [19].

For CFRP bumper plates and aluminium rear wall

$$t_{ob} = t_b = c_b t_w \tag{37}$$

$$t_w = \left[0.866 \frac{d_p K_{3D}^{2/3} \rho_p^{1/3} \rho_{ob}^{1/9} V^{2/3} (\cos\theta)^\delta (70/\sigma_y)^{1/3}}{(c_b + K_{tw})^{2/3} S_1^{1/3} + K_{S2} S_2^\beta (\cos\theta)^{-\varepsilon}} \right]^{3/2} \tag{38}$$

where $c_b = 0.1$ and shield properties (t, σ, ρ) are for a reference aluminium.

$K_{3D} = 0.4; \quad K_{S2} = 1.0; \quad K_{tw} = 1.0$

$\varepsilon = 0; \quad \delta = 4/3; \quad \beta = 1/3; \quad \gamma = 2/3$

For all-aluminium configurations, thicknesses are calculated as

$$t_{ob} = t_b = c_b t_w \tag{39}$$

where $c_b = 0.1$

$$t_w = -\frac{C_1^{-2}}{2}\left(C_2 - \sqrt{C_2^2 + 4C_1 C_3}\right)C_3 - \frac{\left(C_2 - \sqrt{C_2^2 + 4C_1 C_3}\right)}{2C_1^3} - \frac{C_2 C_3}{C_1^2} \tag{40}$$

where $C_1 = 1.368 S_1^{1/3}$

$C_2 = K_{S2} S_2^\beta (\cos\theta)^{-\varepsilon}$

$C_3 = 0.866\, d_p K_{3D}^{2/3} \rho_p^{1/3} \rho_{ob}^{1/9} V^{2/3} \times (\cos\theta)^\delta (70/\sigma_y)^{1/3}$

$K_{3D} = 0.4; \quad K_{S2} = 0.1; \quad K_{tw} = 1.5$

$\delta = \begin{cases} 4/3 & \text{if } 45 \ge \theta \le 65° \\ 5/4 & \text{if } 45 < \theta > 65° \end{cases}$

$\varepsilon = \begin{cases} 8/3 & \text{if } 45 \ge \theta \le 65° \\ 10/4 & \text{if } 45 < \theta > 65° \end{cases}$

$\beta = 2/3; \quad \gamma = 1/3$

As a practical guideline, the accuracy of Eq. (38) is questionable for facesheet thicknesses below 0.04 cm for aluminium and 0.1 cm for CFRP (however, towards this limit sizing is expected to be conservative). Eq. (38) is valid only for impacts in the HV regime (i.e. $V > V_{HV}/\cos\theta$), which is defined as velocities that are above 7, 8.4, and 10 km/s for the impact of al-on-al, CFRP, and MLI, respectively.

The performance of a triple-wall shield is calculated in the low velocity regime, i.e. $V \le V_{LV}\cos\theta$, using

$$d_c = \left[\frac{(t_w^{1/2} + t_b)/K_{3S}(\sigma_y/40)^{1/2} + t_{ob}}{0.6(\cos\theta)^\delta \rho_p^{1/2} V^{2/3}} \right]^{18/19} \tag{41}$$

where $K_{3S} = 1.1$ for CFRP and 1.4 for aluminium and $V_{LV} = 4.2$ for CFRP and 3.0 for aluminium.

In the hypervelocity regime, i.e. $V \ge V_{HV}\cos\theta$,

$$d_c = \frac{1.155\left(S_1^{1/3}(t_b + K_{tw}t_w)^{2/3} + K_{S2} S_2^\beta t_w^\gamma (\cos\theta)^{-\varepsilon}\right)}{K_{3D}\rho_p^{1/3}\rho_{ob}^{1/9}V^{2/3}(\cos\theta)^\delta (70/\sigma_y)^{1/3}} \tag{42}$$

In the intermediate regime, linear interpolation is used. For an overview of the SRL equation validation basis, see Section 3.2.2.

3.4. Advanced configurations

Analysis capability for stuffed Whipple, multi-shock, and mesh double-bumper shields is provided within the programme.

3.4.1. Stuffed Whipple shield

The stuffed Whipple shield includes intermediate fabric layers (such as Nextel ceramic fibre or Kevlar® aramid fibre) between an outer aluminium bumper plate and an inner aluminium pressure wall. These intermediate layers (or stuffing) act to reduce the impulsive load of projectile fragments on the spacecraft pressure hull. For sizing a stuffed Whipple shield, Christiansen [16] defines the following equations:

$$t_b = c_b d_p \rho_p / \rho_b \tag{43}$$

$$AD_{stuffing} = c_{stuffing} d_p \rho_p \tag{44}$$

$$AD_b = t_b \rho_b + AD_{stuffing} \tag{45}$$

$$t_w = c_w \left(\frac{AD_b}{c_0 d_p \rho_p} \right)^{-11/10} \frac{m_p(V\cos^{3/2}\theta)}{\rho_w S^2(\sigma_y/40)^{1/2}} \tag{46}$$

The equation coefficients are given for impact of an aluminium particle on a Whipple shield with Kevlar/Nextel stuffing. Other types of ceramic cloth are also suitable for use with the sizing equations. In the above equations, coefficient $c_b = 0.15$ (unitless), $c_{stuffing} = 0.23$ (unitless), $c_w = 8.8$ (s/km), and $c_0 = 0.38$ (unitless). The Nextel/Kevlar stuffing should be placed halfway between the bumper and plate and rear wall, and the fraction of Nextel to Kevlar areal weight should be kept to: $AD_{Nextel} = 3AD_{Kevlar}$. No limits are placed on shield spacing.

The performance of a stuffed Whipple shield configuration in the low velocity regime, i.e. $V \le 2.6/(\cos\theta)^{1/2}$, is calculated as

$$d_c = 2.35 \frac{(t_w(\sigma_y/40)^{1/2} + 0.37 AD_b)}{((\cos\theta)^{4/3}\rho_p^{1/2}V^{2/3})} \tag{47}$$

In the hypervelocity regime, $V \ge 6.5/(\cos\theta)^{3/4}$,

$$d_c = 0.6 \frac{(t_w \rho_w)^{1/3} S^{2/3}(\sigma_y/40)^{1/6}}{\rho_p^{1/3}V^{1/3}(\cos\theta)^{1/2}} \tag{48}$$

In the intermediate regime, linear interpolation is used.

Given its extensive application on the ISS, the stuffed Whipple shield configuration has been subjected to extensive impact testing. Application of the stuffed Whipple shield BLE is not restricted by shield spacing to projectile

diameter ratio (unlike the MS and mesh double-bumper equations), nor is a limit angle defined.

3.4.2. Multi-shock

Three multi-shock (MS) configurations are considered within the analysis programme, as follows.

- Four equally spaced fabric bumpers with a flexible rear wall,
- Four equally spaced ceramic fabric bumpers with an aluminium rear wall, and
- Two equally spaced ceramic fabric bumpers with a two-sheet aluminium Whipple shield (aka hybrid MS).

The MS equations use a combined bumper areal density AD_b, and total shield spacing S, that are sized accordingly (from Ref. [2])

For a ceramic MS shield with a flexible rear wall,

$$AD_b = 0.19 d_p \rho_p \tag{49}$$

$$AD_w = c_w m_p (V \cos\theta)/S^2 \tag{50}$$

where $c_w = 43.6$ for Nextel and 29.0 for Kevlar.

For a ceramic MS shield with an aluminium rear wall,

$$AD_b = 0.19 d_p \rho_p \tag{51}$$

$$AD_w = 41.7 m_p (V \cos\theta)/S^2 (40/\sigma_y)^{1/2} \tag{52}$$

For a hybrid MS shield,

$$AD_b = 0.5 AD_w \tag{53}$$

$$AD_A = 0.5 AD_w \tag{54}$$

$$AD_w = \frac{0.269 d_p^{3/2} \rho_p^{1/2} \rho_A^{1/6} (V \cos\theta)}{S^{1/2} (\sigma_y/40)^{1/2}} \tag{55}$$

For the Nextel MS shields, no limit angle is defined as the ceramic fabric bumpers are not considered to produce damaging fragments (unlike metallic structures). However, for the hybrid Nextel/aluminium MS shields, a limit incidence of 75° is used.

The performance of the MS shield configurations is assessed over three velocity ranges. In the low velocity regime i.e. $V \leq V_{LV}$:

For a ceramic MS shield with a flexible rear wall,

$$d_c = 2.7 \frac{(0.5 AD_w + 0.37 AD_b)}{((\cos\theta)^{4/3} \rho_p^{1/2} V^{2/3})} \tag{56}$$

For a ceramic MS shield with an aluminium rear wall,

$$d_c = 2 \frac{(t_w (\sigma_y/40)^{1/2} + 0.37 AD_b)}{((\cos\theta)^{4/3} \rho_p^{1/2} V^{2/3})} \tag{57}$$

For a hybrid MS shield,

$$d_c = 2 \frac{(t_w (\sigma_y/40)^{1/2} + 0.37 AD_b)}{((\cos\theta)^{\chi} \rho_p^{1/2} V^{2/3})} \tag{58}$$

where $\chi = 7/3$ when $\theta \leq 45°$ and $\chi = 2$ when $\theta > 45°$.

In the hypervelocity regime, i.e. $V \geq V_{HV}$:

For a ceramic MS shield with a flexible rear wall,

$$d_c = 1.24 \frac{AD_w^{1/3} S^{2/3}}{K^{1/3} \rho_p^{1/3} V^{1/3} (\cos\theta)^{1/3}} \tag{59}$$

where $K = 43.6$ for Nextel and 29.0 for Kevlar.

For a ceramic MS shield with an aluminium rear wall,

$$d_c = 0.358 \frac{(t_w \rho_w)^{1/3} S^{2/3} (\sigma_y/40)^{1/6}}{\rho_p^{1/3} V^{1/3} (\cos\theta)^{1/3}} \tag{60}$$

For a hybrid MS shield,

$$d_c = 2.4 \frac{(t_w \rho_w)^{2/3} S^{1/3} (\sigma_y/40)^{1/3}}{\rho_p^{1/3} \rho_A^{1/9} (V \cos\theta)^{2/3}} \tag{61}$$

In the intermediate regime, linear interpolation is used. The velocity regime limits V_{LV} and V_{HV} are defined as $2.4/(\cos\theta)^{1/2}$ and $6.4/(\cos\theta)^{1/4}$ for Nextel MS shields (fabric or Al rear wall), and $2.7/(\cos\theta)^{1/4}$ and $6.5/(\cos\theta)^{2/3}$ for hybrid MS shields, respectively.

The MS BLEs were developed from impact experiments that were performed with aluminium, ruby, and copper projectiles at velocities ranging from 2.5 to 7 km/s. The placement and areal weight of each bumper shield is expected to affect the capability of the MS shield. These BLEs assume equal spacing and areal weight of the individual bumpers, with the exception of the aluminium bumper plate for the hybrid Nextel/aluminium configuration. The MS ballistic limit equation is only valid for configurations with a total standoff-to-projectile-diameter ratio (S/d_p) that is greater than 15. For values that are less than this, the equation may provide non-conservative predictions.

3.4.3. Mesh double-bumper

The mesh double-bumper (MDB) shield consists of an outer layer of aluminium mesh that is effectively followed by a stuffed Whipple shield. Although other materials have been shown to perform as well or better than aluminium (e.g. graphite/epoxy, Nextel, etc.) for the second bumper, the only configuration that is considered for the MDB ballistic limit equation uses an aluminium plate. The mesh, second bumper plate and intermediate fabric layer are sized for optimal shielding capability and minimal weight in a manner similar to that of the bumper plate of a Whipple shield bumper plate. These components are sized in terms of their areal density, i.e.

$$AD_{mesh} = c_{mesh} d_p \rho_p \tag{62}$$

$$AD_{b2} = 0.093 d_p \rho_p \tag{63}$$

$$AD_b = AD_{mesh} + AD_{b2} \tag{64}$$

$$AD_f = c_f d_p \rho_p \tag{65}$$

$$AD_w = 9 m_p (V \cos\theta)/S^{3/2} (40/\sigma_y)^{0.5} \tag{66}$$

The mesh sizing coefficient, c_{mesh}, can range from 0.035 to 0.057 without affecting the accuracy of the sizing equations for the remaining shield components. A larger value means that a higher percentage of the bumper areal mass is concentrated in the mesh bumper, with a subsequent reduction in the areal mass of the second

bumper plate and intermediate fabric layer. The fabric sizing coefficient, c_f, is given as 0.064 for Kevlar® and Spectra®, and 0.095 for Nextel.

Eqs. (62)–(66) are valid for impact velocities above $6.4/(\cos\theta)^{1/3}$ (i.e. hypervelocity regime), and total shield spacing to projectile diameter ratios (S/d_p) greater than 15. Internal distribution of the shield bumpers should be made such that S_1 (mesh bumper to second plate)$=4d_p$, and S_3 (fabric layer to rear wall)$=4d_p$.

The performance of a MDB shield in the low velocity regime, i.e. $V \le 2.8/(\cos\theta)^{1/2}$ is determined as

$$d_c = 2.2 \frac{(t_w(\sigma_y/40)^{1/2} + 0.37(AD_b + AD_f))}{((\cos\theta)^{5/3}\rho_p^{1/2}V^{2/3})} \tag{67}$$

In the hypervelocity regime, i.e. $V \ge 6.4/(\cos\theta)^{1/3}$,

$$d_c = 0.6 \frac{(t_w\rho_w)^{1/3}S^{1/2}(\sigma_y/40)^{1/6}}{\rho_p^{1/3}(V\cos\theta)^{1/3}} \tag{68}$$

In the intermediate regime, linear interpolation is used.

Over 100 HV impact tests have been performed by NASA JSC on MDB shield configurations. However, these tests included material and spacing investigations and, as such, all were not used for derivation and empirical adjustment of the BLE. The equations are validated for configurations using either Kevlar® or Spectra® for the intermediate fabric layer. Although the placement of the fabric layer was found to have a significant influence on shielding capability, the equation considers only the total spacing of the shield. The equation was derived using fabric layers that were located at a short distance (three to four times the projectile diameter) from the rear wall.

3.5. Thermal Protection Systems (TPS)

Analysis capability is provided for the following types of TPS within the programme: ceramic tile (e.g. LI-900, AETB-8), reinforced carbon–carbon (RCC), and ablator (Avcoat, PICA).

3.5.1. Ceramic tiles

Two types of ceramic tiles are used on board the shuttle: standard low (LI-900) and higher-density (LI-2200). The tiles are composed of compacted silica fibres that are fused with colloidal silica during a high-temperature sintering process. The tiles have a borosilicate coating on top and at sides that is nominally 0.20–0.38 mm thick. The rear surface is bonded with room temperature vulcanising (RTV) adhesive to a strain isolation pad (SIP) that is then bonded to the vehicle skin (monolithic plate or honeycomb sandwich panel). Aluminium enhanced thermal barrier (AETB) tiles with toughened unipiece fibrous insulation (TUFI) coating were developed at NASA Ames Research Centre as an improvement to the LI-900 tile. The AETB-8 tiles are also coated on the top and sides by a borosilicate glass layer, and are bonded to a 0.4 cm-thick SIP and a graphite-cyanate composite facesheeted sandwich panel.

The penetration depth into ceramic tiles that are bonded to a SIP and a substructure (monolithic plate or honeycomb sandwich panel) is calculated using (from Ref. [20]) as,

$$P_\infty = Kd_p(V\cos\theta)^{2/3}(\rho_p/\rho_T)^{1/2} \tag{69}$$

where ρ_T is the nominal density of the ceramic tile (not including glass coating or ceramic slurry used for densification) and is equal to $0.24/0.14/0.35$ g/cm^3 for the AETB-8/LI-900/LI-2200 tile.

$K=1.177$ for the AETB-8 tiles, and 1.27 for the LI-type tiles.

For stand-alone tiles, thickness is defined in terms of allowable penetration depth (as a percentage of the tile thickness), P_c, i.e.

$$t_T = \frac{K}{P_c}d_p(V\cos\theta)^{2/3}(\rho_p/\rho_T)^{1/2} \tag{70}$$

The ballistic performance of unsupported tiles is calculated as:

$$d_c = P_cKt_T(V\cos\theta)^{-2/3}(\rho_p/\rho_T)^{-1/2} \tag{71}$$

where $K=0.79$ and 0.85 for the LI and AETB-8 tiles.

For the LI-900 and LI-2200 tiles, general ballistic limit equations were derived in Ref. [20] to predict the critical projectile diameter resulting in the threshold perforation of a TPS tile and substructure (either monolithic plate or honeycomb sandwich panel). As the ceramic tiles are bonded to the SIP and metallic substructure, detached spallation from the rear of the tile is not applicable. As such, the onset of failure is defined once perforation of the substructure occurs. For the following equations, the wall thickness t_w is the plate thickness, or sum of the two honeycomb facesheet thicknesses, depending on the substructure type.

For low velocity impacts, i.e. $V \le 2.5\cos\theta$,

$$d_c = \frac{t_w(\sigma_y/40)^{1/2} + t_T(\rho_T/\rho_{Al})^{1/2}}{0.55(\cos\theta)^{5/3}\rho_p^{1/2}V^{2/3}} \tag{72}$$

For hypervelocity impacts, i.e. $V \ge 7\cos\theta$,

$$d_c = 3\frac{(t_T + 0.5t_{HC})^{1/3}(t_{w+SIP})^{2/3}(\sigma_y/70)^{1/3}}{\rho_p^{1/3}(V\cos\theta)^{2/3}} \tag{73}$$

where $t_{w+SIP} = t_w + AD_{SIP}/\rho_w$

For intermediate velocity impacts, linear interpolation is used.

For supported AETB-8 tiles, a ballistic limit equation is presented in Ref. [9] for configurations with a composite facesheeted honeycomb sandwich panel substructure. Failure is defined as any hole or through crack in the rear facesheet of the honeycomb sandwich panel. For low velocity impacts, i.e. $V \le 2.5\cos\theta$,

$$d_c = 2.64\rho_p^{-1/2}(\cos\theta)^{-5/3}V^{-2/3} \tag{74}$$

For impacts at hypervelocity, i.e. $V \ge 7\cos\theta$,

$$d_c = 2.98\rho_p^{-1/3}(V\cos\theta)^{-2/3} \tag{75}$$

For intermediate velocity impacts, linear interpolation is used.

In addition to penetration, the size of non-penetrating craters in ceramic tiles is also of concern (particularly in the wake of the Columbia accident). During re-entry, non-penetrating impact craters can grow until they reach the

substructure (plate or honeycomb), effectively resulting in a penetration-type failure. For this, the maximum cavity diameter is of interest as it is generally larger than the entry hole with ceramic tiles. The maximum cavity diameter, D_c, is calculated as (from Ref. [21])

$$D_c = 1.85 d_p \rho_p^{1/3} V^{2/3} (1 + 0.25 \sin \theta)^{2/3} \tag{76}$$

To evaluate the impact performance of ceramic TPS tiles when using maximum cavity size as a failure criterion, the critical projectile diameter is calculated in terms of a user-defined maximum allowable cavity diameter $D_{c,\ max}$ as

$$d_c = \frac{D_{c,\text{max}}}{1.85 \rho_p^{1/3} V^{2/3} (1 + 0.25 \sin \theta)^{2/3}} \tag{77}$$

The general penetration-based TPS ballistic limit equation was derived using test data from 12 impact experiments on TPS configurations with 4 mm-thick SIP bonded to aluminium plates and aluminium honeycomb sandwich panels. The impact tests were performed with aluminium and steel spheres, at different impact angels (0°, 30°, 45°, and 60°) over a range of impact velocities from 2.65 to 7.42 km/s. The aluminium plate had a thickness of 0.25/0.13 cm, and the dimensions of the aluminium honeycomb sandwich panel were 0.064 cm-thick facesheets and 2.5 cm-thick core. For entry hole diameter-based equations, additional impact tests (including some on tile samples that had no supporting substructure or borosilicate glass coating) were considered [22]. The ballistic limit equation for AETB tiles and substrate are significantly less widely validated, based on limited normal incidence testing on the X-38 crew return vehicle (CRV) TPS. These tests were performed on a 5.1 cm-thick tile that is bonded to a 0.4 cm thick SIP and 3.8 cm thick honeycomb sandwich panel with 0.2 cm thick graphite/cyanate facesheets.

3.5.2. Reinforced carbon–carbon (RCC)

RCC is a structural composite that is used as the TPS for the high-temperature areas of the shuttle; i.e. the wing leading edge and the nose cap. To meet the requirements for oxidation resistance and reusability, the RCC is coated with silicon carbide (SiC), as shown in Fig. 4.
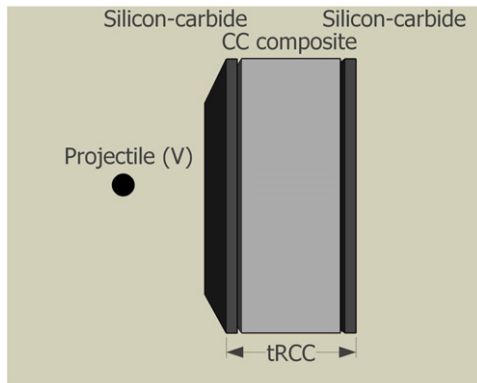

Fig. 4. RCC TPS configuration for BLE analysis.

The ballistic limit of RCC is calculated using a cratering equation in which the penetration depth is determined using (from Ref. [20])

$$P_\infty = 0.61 d_p (V \cos \theta)^{2/3} (\rho_p / \rho_{RCC})^{1/2} \tag{78}$$

Similar to the Cour-Palais cratering equation for metallic plates, the failure limits of RCC are determined by reducing the thickness of the semi-infinite plate applicable in Eq. (78). The required thickness of RCC to prevent failure can be calculated using

To prevent detached spall $t_{RCC} \geq 4.5 P_\infty$ (79)

To prevent perforation $t_{RCC} \geq 2.3 P_\infty$ (80)

To assess the performance of RCC, the ballistic limit equation is defined as

$$d_c = 1.639 \frac{t_{RCC} (\rho_{RCC} / \rho_p)^{1/2}}{k (V \cos \theta)^{2/3}} \tag{81}$$

where $k = 2.3$ for penetration and 4.5 for detached spall.

The diameter of perforation holes in RCC is critical to its thermal protective capability. The hole diameter in completely perforated RCC panels is measured as the through-hole diameter (not entry or exit diameter, as shown in Fig. 5) and is calculated using

$$D_h = 2.2 d_p \rho_p^{1/3} (V \cos \theta)^{1/3} - 0.36 \tag{82}$$

For allowable clear hole diameter-based sizing of RCC panels, Eq. (82) is solved for projectile diameter, d_p, in terms of $D_{h,\text{max}}$, which is then substituted into the sizing equation for no perforation i.e.

$$t_{RCC} = \frac{1.342 (V \cos \theta)^{1/3} (D_{h,\text{max}} + 0.36)}{\rho_p^{1/3} (\rho_{RCC} / \rho_p)^{1/2}} \tag{83}$$

To evaluate the performance of an RCC panel over a range of impact conditions that is based on maximum allowable perforation hole diameter, a three-step procedure is applied as follows.

(1) The clear hole diameter (D_h) is calculated at the onset of perforation (i.e. $d_p = d_c$) over the range of relevant impact velocities using Eqs. (81) and (82).
(2) A maximum clear hole diameter ($D_{h,\text{max}}$) that is greater than those calculated in step 1) is defined for the range of impact velocities considered.
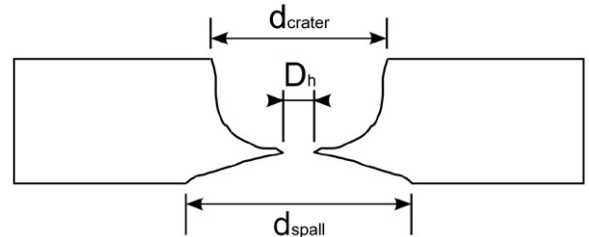(3) The critical projectile diameter is calculated for the applicable range of impact velocities (i.e. ballistic

Fig. 5. Clear hole diameter measurement in RCC.

limit curve) in terms of $D_{h,\max}$,

$$d_c = \frac{D_{h,\max} + 0.36}{2.2\rho_p^{1/3}(V\cos\theta)^{1/3}} \tag{84}$$

It should be noted that clear hole diameter characterisation has been performed for 6.3 mm, nominally thick RCC panels (with 0.8 mm-thick SiC coating on the upper and lower surfaces). The effect of panel thickness on perforation hole diameter is unknown and, as such, application of hole diameter-based failure limits for structures with thicknesses other than 6.3 mm should be made with caution.

Eq. (78) has been developed from a series of nine impact tests [20]. Recent updates to RCC damage equations have been developed at NASA JSC as part of the shuttle return to flight investigation; however, these results have focused primarily on failure limits (i.e. allowable crater dimensions) rather than on penetration thresholds.

3.5.3. Ablative heat shield

Penetration equations have been developed for two types of ablative shields: Avcoat and phenolic impregnated carbon ablator (PICA). Avcoat is low-density, glass-filled epoxy-novolac that was used as an ablative heat shield during the Apollo Programme. PICA is a combination of carbon fibreform and phenolic resin, and is a lightweight alternative to Avcoat (nominal density of 0.24 g/cm³). High-density PICA is also available, with a nominal density of 0.48 g/cm³. Penetration into porous, low-density ablative materials by MMOD projectiles forms a central damage cavity; however, in some cases individual projectile fragments may penetrate beyond the central cavity. The depth of these individual fragment channels are not predicted by the penetration equations.

The penetration into an ablative heat shield is calculated using (from Ref. [7,9])

$$P_\infty = Kd_p^{\alpha}\rho_p^{1/2}(V\cos\theta)^{2/3} \tag{85}$$

where $K = 1.61$, 1.25 for Avcoat ($\rho_p/\rho_{AC} > 4$ and $\rho_p/\rho_{AC} \le 4$, respectively), and $K = 0.72\rho_s^{-0.92}$ for PICA and $\alpha = 1.06$ for Avcoat and 0.85 for PICA.

Allowable penetration limits into an ablative heat shield such as Avcoat are not fully characterised and may be mission dependant. As such, failure limits are defined by the user in terms of the failure coefficient k, i.e.

$$t_s = kP_\infty \tag{86}$$

where $k = 100/P_{\text{allowable}}$ and $P_{\text{allowable}}$ is expressed as a percentage.

The ballistic performance of an ablative heat shield is calculated using

$$d_c = \left[\frac{t_s}{kK\rho_p^{1/2}(V\cos\theta)^{2/3}}\right]^{1/\alpha} \tag{87}$$

The Avcoat penetration equation was empirically adjusted from the general Cour-Palais cratering equation based on extensive testing performed during the Apollo Programme at NASA JSC, General Motors Defence Research Laboratory, AVCO, and the Naval Research Laboratory (NRL).

PICA is being considered for use on the Orion CEV, for which test data is not publicly available.

3.6. Shape effects

All BLEs defined hereto are valid for the impact of solid spherical projectiles. Although it is generally considered that spherical projectiles can reasonably represent meteoroids, this is not true for orbital debris [23]. Rod- ($L/D > 1$) and disc- ($L/D < 1$) shaped projectiles have both been found to be more lethal on impact with a dual-wall shield at HV than a comparable spherical projectile [24]. This is because a considerable percentage of the projectile mass remains a lethal threat to the rear wall following perforation of the bumper plate. As such, current ballistic limit curves are effectively based on impact from the most benign of projectile shapes at normal orientation (i.e. not considering cylindrical projectiles inclined off their rotational axis). Thus, the equations that were presented in the preceding sections may inherently provide a non-conservative estimation of penetration risk. Schaefer et al. [25] considered the effect of projectile shape on the penetration risk of metallic Whipple shields in terms of rotationally symmetrical ellipsoids (semi major axis $a = b \ne c$), shown in Fig. 6. The advantage of this approach is that the projectile shape can be described in terms of a single parameter f, which is effectively equal to the L/D ratio of a cylindrical projectile (i.e. $f = c/a$). A projectile is therefore described either as spherical ($f = 1$), oblate ($f < 1$), or prolate ($f > 1$).

For impact on a metallic Whipple shield, the shape effect is taken into account in the LV regime by incorporating the shape factor f^{a2} into the equation denominator. For example, in the LV regime (i.e. $V/\cos\theta \le V_{LV}f^{a1}$ km/s), the shape factor-modified Whipple shield BLE (Eq. (30)) is expressed as

$$d_c = \left[\frac{t_w(\sigma_y/40)^{1/2} + t_b}{0.6(\cos\theta)^{5/3}\rho_p^{1/2}V^{2/3}f^{a2}}\right]^{18/19} \tag{88}$$

where $a1 = 0.08$; $a2 = 0.30$

In the HV regime (i.e. $V/\cos\theta \ge V_{HV}f^{b1}$ km/s), projectile shape is accounted for by the inclusion of a Gaussian
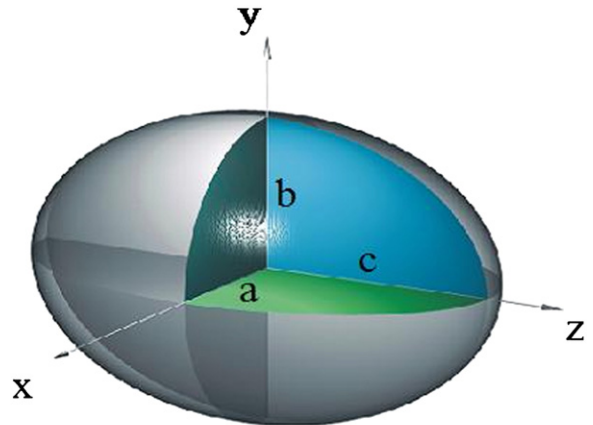

Fig. 6. Ellipsoid with rotational symmetry.

function and shape factor f^{b2}

$$d_c = 3.918 F_2^* \frac{t_w^{2/3} S^{1/3} (\sigma_y/70)^{1/3}}{\rho_p^{1/3} \rho_b^{1/9} (V\cos\theta)^{2/3}} \frac{f^{b1}}{b3^{(f-1)^2/b2}} \qquad (89)$$

where $b1=0.25$; $b2=0.4$; $b3=1.4$ and $b2=0.4$.

For impact velocities in the intermediate regime, the effect of projectile shape is considered to vary the fragmentation behaviour of the impacting projectile (i.e. the onset of projectile breakup and projectile melting). This effect is accounted for the inclusion of the shape factor f^{a1} for V_{LV} and f^{b1} for V_{HV}, in addition to the empirically adjusted fit factors $a1$ and $b1$, such that the linear interpolation between Eqs. (88) and (89) remains valid.

By considering non-spherical projectiles, it is evident that the definition of critical projectile diameter is no longer directly applicable. More appropriately, failure limits that are based on projectile "critical mass" can be calculated from Eqs. (88)–(89) as

$$m_c(V) = \rho_p \frac{\pi}{6} (d_c(V))^3 \qquad (90)$$

Nonetheless, current risk assessment software (e.g. BUMPER, ESABASE, etc.) requires ballistic limit equations that are expressed in terms of projectile diameter. Thus, for non-spherical particles, failure limits are expressed in terms of a mass-equivalent spherical diameter.

The ballistic limit modifications for unyawed ellipsoid projectiles were derived from experimental and numerical impact data using three different projectile volumes (equivalent to 6, 5, and 4 mm diameter aluminium spheres) with three different shape factors ($f=0.42$, 1.0, and 1.53). In total, 39 impact tests were performed, all at normal incidence, over impact velocities ranging between 0.85 and 6.76 km/s. Eight hydrocode simulations were performed that considered only impact of the prolate ellipsoid ($f=1.53$) at impact velocities between 0.5 and 13.0 km/s. All impact tests and simulations were performed on aluminium Whipple shield targets.

3.7. Multi-layer insulation (MLI)

In practise, MLI is included in the majority of shielding configurations either as an internal layer of the shield or placed externally on the outer most bumper plate. The presence of MLI can significantly affect, both positively and detrimentally, the impact performance of shielding configurations at hypervelocity [26]. Currently there is no all-encompassing means to predict the effect of MLI on the performance of a debris shield. Indeed, most damage equations do not allow for the inclusion of MLI. For MLI that is located on the exposed surface of a monolithic metal shield, an increase in penetration limit is predicted based on cratering relationships (from Ref. [9])

$$d_{c,MLI} = 2.2 AD_{MLI} \rho_p^{-0.47} (V\cos\theta) - 0.63 + d_{c,no\ MLI} \qquad (91)$$

For MLI that is placed on the outer surface of monolithic composite shields, Schaefer et al. [5] defined an increase in penetration limit corresponding to an effective increase in shield thickness as

$$t_{s,eff} = t_s + K_{MLI} \frac{AD_{MLI}}{\rho_s} \qquad (92)$$

where $K_{MLI}=4.5$ for monolithic composites.

For multi-wall configurations, the effect of MLI that is placed on the outer surface of the external bumper is characterised in a similar manner to Eq. (92), however the constant K_{MLI} is equal to 3.0 (from Ref. [18]). For MLI placed between the bumper and rear wall, Christiansen [16] proposes an increase in critical diameter that is a function of the MLI areal density (AD_{MLI}), and distance from the bumper plate (S_{MLI}), i.e.

$$d_{c,MLI} = d_{c,no\ MLI} + \Delta_{MLI} \qquad (93)$$

where $\Delta_{MLI} = K_{MLI} AD_{MLI}(S_{MLI}/S)^{1/2}$ and $K_{MLI}=1.4$ cm^2.

With caution, these approaches can be included in any of the single- and multi-wall ballistic limit equations (excluding the advanced configurations) that are presented in this paper for preliminary sizing or performance evaluation of an MMOD shield. However, their validity is not widely developed and, thus, the predictions may be non-conservative (e.g. ATV-ICC [27]).

4. Summary

A simple programme has been developed to enable fast and accurate utilisation of ballistic limit equations (BLEs) in preliminary shield design and performance assessment. The programme runs as an add-in to Microsoft Excel®, and is fully controlled via a graphical user interface (GUI). Capability has been provided within the programme for analysis of single wall (metallic, composite, and transparent), dual-wall (Whipple shield, honeycomb core and sandwich panel), triple-wall, advanced (stuffed Whipple, multi-shock, and mesh double-bumper), and thermal (ceramic tile, reinforced carbon-carbon, ablator) protection systems. Further extensions for non-spherical projectiles and multi-layer insulation (MLI) are included, although the validation of these techniques is limited, and therefore should be used with caution. The BLEs applied for each configuration have been selected (in the case of multiple possibilities) through a competitive evaluation against existing test data. Their selection, however, should not be considered as an endorsement by NASA Johnson Space Centre or the Hypervelocity Impact Technology Facility (HITF) in any way. It is intended that further updates to the program will be made in light of new developments in BLE capability.

References

[1] R. Destefanis, et al., Selecting enhanced space debris shields for manned spacecraft, International Journal of Impact Engineering 33 (2006) 219–230.

[2] E.L. Christiansen, Design and performance equations for advanced meteoroid and debris shields, International Journal of Impact Engineering 14 (1–4) (1993) 145–156.

[3] B. Cour-Palais, Meteoroid protection by multiwall structures, in: Proceedings of the Hypervelocity Impact Conference AIAA, Cincinnati, 1969.

[4] G. Drolshagen, J. Borde, Meteoroid/Debris Impact Analysis (ESA-BASE/DEBRIS), ESA ESTEC, 1992.

[5] F. Schaefer, E. Schneider, M. Lambert, Review of ballistic limit equations for CFRP structure walls of satellites, in: Proceedings of the Fifth International Conference on Environmental Testing for Space Programs, Noordwijk, 2004.

[6] S. Ryan, E. Christiansen, Micrometeoroid and orbital debris (MMOD) shield ballistic limit analysis program, NASA Johnson Space Center, NASA/TM-2009-214789, Houston, 2010.

[7] B. Cour-Palais, Empirical hypervelocity equations developed for Project Apollo, OART Hypervelocity Impact Workshop, Houston, 1968.

[8] M. Ratliff, Single-Wall Equation for Titanium Shield in James Webb Space Telescope [JWST] Integrated Science Module (ISIM) Electrical Cable Protection, NASA Engineering and Safety Center, 2008.

[9] E. Christiansen, et al., Handbook for Designing MMOD Protection, NASA Johnson Space Center, NASA/TM-2009-214785, Houston, 2009.

[10] F. Lyons, S. McMurray, E. Christiansen, Return to Flight (RTF) Hypervelocity Impact Testing on Impact Penetration Sensor System (IPSS)—Medium and High Fidelity Testing on Fiberglass and Reinforced Carbon–Carbon Panels, NASA Johnson Space Center, JSC-62803, Houston, 2005.

[11] B. Cour-Palais, Hypervelocity impact investigations and meteoroid shielding experience related to Apollo and Skylab, Orbital Debris (1982) 247–275.

[12] S. Ryan, Ballistic Limit Equation for Fused Quartz Glass, NASA Johnson Space Center, Houston, 2008.

[13] K. Edelstein, Hypervelocity impact damage tolerance of fused silica glass, in: Proceedings of the 43rd International Astronautical Congress, Washington DC, 1992.

[14] R. Burt, E. Christiansen, Hypervelocity impact testing of transparent spacecraft materials, International Journal of Impact Engineering 29 (2003) 153–166.

[15] H. Reimerdes, D. Noelke, F. Schaefer, Modified Cour-Palais/Christiansen damage equations for double-wall structures, International Journal of Impact Engineering 33 (1–2) (2006) 645–654.

[16] E. Christiansen, Meteoroid/Debris Shielding, NASA Johnson Space Center, NASA/TP-2003-210788, Houston, 2003.

[17] S. Ryan, et al., A ballistic limit equation for hypervelocity impacts on CFRP/Al HC satellite structures, Advances in Space Research 41 (2008) 1152–1166.

[18] F. Schaefer, et al., Ballistic limit equation for equipment placed behind satellite structure walls, International Journal of Impact Engineering 35 (2008) 1784–1791.

[19] R. Putzar, et al., Vulnerability of Spacecraft Equipment to Space Debris and Meteoroid Impacts, Ernst-Mach-Institute, EMI I-15/06, Freiburg, 2006.

[20] E. Christiansen, L. Friesen, Penetration equations for thermal protection materials, International Journal of Impact Engineering 20 (1–5) (1997) 153–164.

[21] E. Christiansen, B. Cour-Palais, L. Friesen, Extravehicular activity suit penetration resistance, International Journal of Impact Engineering 23 (1999) 113–124.

[22] E. Christiansen, J. Ortega, Hypervelocity impact testing of shuttle orbiter thermal protection system tiles, in: Proceedings of the AIAA Space Programs and Technologies Conference, Huntsville, 1990.

[23] B. Cour-Palais, The shape effect of non-spherical projectiles in hypervelocity impacts, International Journal of Impact Engineering 26 (1–10) (2001) 129–143.

[24] A. Piekutowski, Debris Clouds Produced by the hypevelocity Impact of Nonspherical Projectiles, International Journal of Impact Engineering 26 (2001) 613–624.

[25] F. Schaefer, S. Hiermaier, E. Schneider, Ballistic limit equation for the normal impact of unyawed ellipsoid-shaped projectiles on aluminum Whipple shields, in: Proceedings of the 54th International Astronautical Congress, Bremen, 2003.

[26] R. Destefanis, et al., Enhanced space debris shields for manned spacecraft, International Journal of Impact Engineering 29 (2003) 215–226.

[27] F. Schaefer, L. Guenther, Impact Testing of ATV-ICC Meteoroid and Debris Protection Shield, Fraunhofer-Institut fuer Kurzzeitdynamik, Ernst-Mach-Institute, EMI E-28/2000 Freiburg, 2001.